Contents lists available at ScienceDirect

Tribology International

journal homepage: www.elsevier.com/locate/triboint

Optimization of surface textures in hydrodynamic lubrication through the adjoint method

A. Codrignani [a],[b],[*], D. Savio [c], L. Pastewka [a], B. Frohnapfel [b], R. van Ostayen [d]

[a] *Department of Microsystems Engineering, University of Freiburg, Freiburg, Germany*
[b] *Institute of Fluid Mechanics, Karlsruhe Institute of Technology, Karlsruhe, Germany*
[c] *Microtribology Center μTC, Fraunhofer Institute for Mechanics of Materials IWM, Freiburg, Germany*
[d] *Department of Precision and Microsystems Engineering, Delft University of Technology, Delft, The Netherlands*

ARTICLE INFO

ABSTRACT

In this work we assess the applicability of the adjoint optimization technique for determining optimal surface topographies of two surfaces in relative motion in presence of a thin lubricant films that can cavitate. Among the existing numerical tools for topology optimization in engineering problems, the adjoint method represents a promising and versatile technique, which can also be applied to the field of full film tribology. In particular, the design of surfaces with complex textures can thoroughly benefit from this method, as it allows dealing with a large number of degrees of freedom at low computational cost. We show that this optimization method can be successfully applied to cavitating lubricant flows such as in pin-on-disc tribometers, giving the possibility to extend the results also to other typical applications such as journal and slider bearings. It is shown that the adjoint method can optimize the whole gap height distribution point by point in a more efficient way than traditional optimization approaches and parametric studies. In particular, thanks to the sensitivity analysis the adjoint method is able to find the placement and depth profile of each texture element.

1. Introduction

Improvements in the efficiency and reliability of tribological devices are often achieved through shape optimization of the sliding contacts either by modifications of the global contact geometry (*e.g.* optimized Rayleigh step or slider bearing [1,2]) or locally by the introduction of surface textures [3]. The typical goal of the optimization process in hydro-dynamically lubricated contacts is to increase the separation between the sliding surfaces in order to reduce friction and wear. This goal is achieved by increasing the hydrodynamic pressure generated in the contact through the shape optimization of the surfaces. Shape optimization opens the way to potentially infinite variations of surface modifications. For this reason, different optimization techniques have been proposed in literature, which can be categorized in two main groups: optimization techniques based on parametric studies and optimization techniques based on other more sophisticated optimization approaches.

The first group comprises the vast majority of literature, since the shape of the geometry modifications is often parameterized by using elementary shapes, both for textured or stepped surfaces [4]. This is because the complexity of a free-form optimization of the whole gap height distribution $h(\vec{x})$ is usually reduced through elementary shapes

or piecewise approximation of the investigated geometry. For example Rohde [5] as well as Shen & Khonsari [6] maximized the load carrying capacity of a stepped surface for a 2D slider bearing by parametrizing the width, the depth and the position of a Rayleigh step.

Many other researchers focused on parametric studies, in particular for the analysis of surface textures. Since the early works of Etsion and coworkers [3,7] the parametric approach has been the widely used for the optimization of textures in several kind of application, such as 1D slider bearings [8,9], 2D slider bearings [10], Piston–Liner Contacts [11,12], thrust bearings [13] and pin-on-disc tribometers [14]. In some cases, the optimization of surface texture for 1D slider bearings has been also performed by means of analytical solutions [15–17]. It is important to notice that most of the studies on both textured and stepped surfaces always proved the well known theoretical result that the stepped geometry (*i.e.* a redesign of the global surface/contact geometry) performs better than any other textured case. In particular the work of Fillon and Dobrica [18] states the importance of texturing in the same region of the bearing where a Rayleigh step should be.

In the second group more complex optimization strategies have been employed. For example Guzek et al. optimized a 2D parallel bearing with the aid of quadratic programming, hence exploiting the

gradient of the cost function in order to reach the optimal design faster than with usual trial and error approaches [19]. Their method, however, focused on the optimization of predetermined texture topology such as rectangular or elliptical dimples. For this reason other methods based on the optimization of arbitrary shapes have been proposed. Among them Fesanghary and Khonsari [20] applied a hybrid optimization algorithm based on sequential quadratic programming and harmony search to a slider bearing with groove shapes approximated through splines. As a result, a higher load carrying capacity was obtained than through elementary groove shapes. This hints to the fact that an increase in the number of parameters in the optimization algorithm, which in the extreme is equivalent to a point by point optimization of the whole geometry, will perform better than an optimization algorithm based on a reduced number of parameters, such as an optimization of the surface topology described by a set of elementary shapes. Similar conclusions were found also in the work of Wang et al. [21] where elliptical air bearings are optimized by modifying the whole surface in a continuous way thanks to an automated mesh generation. Other strategies for the free-form optimization of the gap height have been proposed by Maday using calculus of variations in the case of a 1D journal bearing [22,23]. Beside the optimization based on the simple Reynolds equation, sequential quadratic programming was also used by Alyaqout and Elsharkawy [24] for slider bearings in the frame of thermo-hydrodynamic lubrication by the coupling of the Reynolds and energy equations.

More generally, optimization strategies share the common concept of sensitivity analysis, that is, looking for the direct relationship between variations in the design parameter space and the corresponding changes in the object function (*i.e.* the function which describes the performance to be achieved). Sensitivity analysis is furthermore at the heart of optimization methods which fall under the category of Lagrangian based methods and adjoint methods [25]. The main advantage of such methods is the possibility of optimizing the whole gap height distribution $h(\vec{x})$ without assigning any predetermined topology modification. This is in contrast to what is done in a typical optimization study based on a parametric geometry.

The adjoint method takes advantage of the Lagrangian formulation in order to define a second partial differential equation which is referred to as the adjoint equation. The solution of the adjoint equation allows to compute the sensitivity in an efficient way, hence knowing the impact of modifications of every single grid point on the objective performance. The adjoint method was first introduced in control theory [26] and then successfully applied in the aerospace sector for the optimization of complex shapes under the fulfillment of the Navier–Stokes equations [27–29]. The first usage of the adjoint method for tribological application was performed by Yoon and Choi [30] for the optimization of an air bearing for hard disks showing a huge reduction in computational cost compared to traditional parametric approaches. Subsequently, the adjoint method was employed for the first time by Van Ostayen [31,32] for the optimization of the load carrying capacity of hydrodynamic slider bearings with particular attention also to the shape optimization under unsteady conditions.

In the current work we present an extension of the work by Van Ostayen and employ the adjoint optimization for the free-form optimization of both the macroscopic geometry and surface textures. To the authors' knowledge, the optimization is carried out for the first time under the constraint of the incompressible Reynolds equation with mass-conserving cavitation. Both the continuous and the discrete formulation of the adjoint method have been implemented under two different computational environments (Comsol® [33] and Matlab®). The validation of the optimization algorithm is first performed against analytical 1D solutions and subsequently between the two different implementations because of the lack of analytical solutions in the presence of cavitation. In order to ease the occurrence of cavitation we choose to test the optimization algorithm on the geometry of a pin-on-disc tribometer. This choice has the additional advantage to provide useful insights for future experimental activities.

The goal of the optimization is to achieve the maximum fly height for a given load since this results in an increase of the gap height and hence in a reduction of friction by bringing the transition from mixed lubrication to hydrodynamic lubrication to a lower sliding speed, as pointed out in several studies [6,34]. Moreover the adjoint method allows to freely find the optimal depth distribution inside the texture elements, giving the possibility to compute the optimal shape of texture elements according to their position on the macro geometry in a much more efficient way than traditional methods [35].

2. Numerical approach

The present optimization problem deals with the thin lubricant film between two surfaces in relative motion. The lubricant flow is described by a set of Partial Differential Equation (PDE) which describes the mass and momentum conservation of a lubricant fluid subjected to cavitation. The optimization problem treats the PDE set as a constraint. In this section we present the formulation of the adjoint method applied to the Reynolds equation with mass-conserving cavitation.

2.1. Governing equation

Under the assumption of an incompressible Newtonian fluid and a sufficiently regular gap height distribution $h(\vec{x})$, the shear flow between two sliding walls can be modeled through the incompressible Reynolds equation in the following form [36]:

$$g(\bar{p}, \theta, h) \equiv \nabla \cdot \left[-\frac{h^3}{12\mu} \nabla \bar{p} + \frac{1}{2}\vec{V} h (1 - \theta) \right] = 0 \tag{1}$$

Here, $\bar{p}(\vec{x}) = p(\vec{x}) - p_{cav}$ is the pressure relative to the cavitation pressure p_{cav}, μ is the dynamic viscosity, $\vec{V} = \{U, W\}^T$ is the upper wall velocity and $\theta(\vec{x})$ is the cavity fraction. As proposed by Elrod and Adams [37] the cavity fraction can be expressed as a function of the local density $\rho(\vec{x})$ of the flow

$$\theta(\vec{x}) = 1 - \frac{\rho(\vec{x})}{\rho_{ref}}. \tag{2}$$

where ρ_{ref} describes the reference density of the lubricant. In this way the cavity fraction is defined to be $\theta = 0$ where the flow is completely in the liquid state and has a maximum value of $\theta = 1$ when the flow is completely in the vapor phase. On the other side, the relative pressure $\bar{p}$ is zero in the cavitation region and positive elsewhere. These two observations can be combined in a single condition which expresses the complementarity constraint of Eq. (1):

$$\left(p - p_{cav} \right) \theta = \bar{p}\theta = 0. \tag{3}$$

Instead of solving Eqs. (1) and (3) in an iterative way, Woloszynski et al. proposed an algorithm which directly couples both equations in a single system [36]. Besides ensuring mass conservation, the coupled solution also has the advantage of being noticeably faster than previous iterative methods [38–40].

The first step in the derivation of such an algorithm is to rewrite the constraint equation (3) using the Fischer–Burmeister equation, so that:

$$f(\bar{p}, \theta) \equiv \bar{p} + \theta - \sqrt{\bar{p}^2 + \theta^2} = 0. \tag{4}$$

After the discretization, the system of equations f and g can be combined in a single system, whose non-linearity can be addressed by applying the Newton–Raphson algorithm. The system of Eqs. (1) and (4) is completed by assigning the pressure and cavity fraction values on the Dirichlet boundaries Σ_D and by assigning the flux $\hat{n} \cdot [-\frac{h^3}{12\mu}\nabla \bar{p} + \frac{1}{2}\vec{V} h(1 - \theta)] = q$ on the Neumann boundaries Σ_N. The resulting normal force, which is also referred to as the load carrying capacity, is given by:

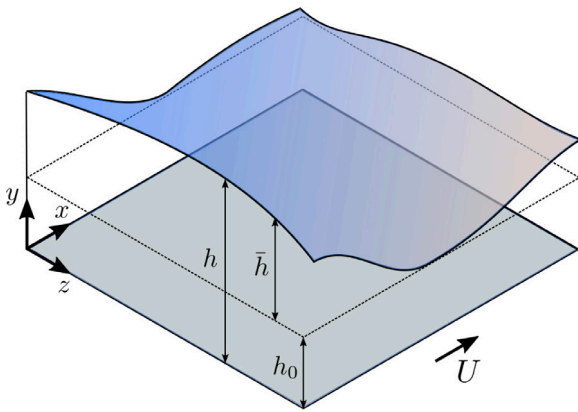$$W = \int_{\Omega} \left(p(\vec{x}) - p_{ext} \right) d\Omega \tag{5}$$

Fig. 1. Sketch of the generic geometry and the coordinate system.

where p_{ext} represents the external pressure acting on the other side of the wall. The tangential force at $y = h$ is computed as [36]

$$\vec{F}_T = \int_{\Omega} \left[\frac{h}{2} \nabla p + (1 - \theta) \mu \frac{\vec{V}}{h} \right] d\Omega, \tag{6}$$

where Ω is the surface area in the $x - z$ plane (see Fig. 1).

2.2. Optimization through the adjoint method

The optimization of hydrodynamic bearing has typically two objectives: either the maximization of the load carrying capacity or the minimization of the friction coefficient. The two objectives may lead to different optimal shapes as highlighted among others by Rahmani et al. [41]. In this work we focus on the first objective, since a higher load carrying capacity can also reduce friction indirectly due to the increase in the overall gap height [2]. For this reason we can formulate our optimization problem as follows:

$$
\begin{aligned}
\underset{h(\vec{x})}{\text{maximize}} \quad & f_{\text{obj}} = W = \int_{\Omega} \left(p(\vec{x}) - p_{\text{ext}} \right) d\Omega \\
\text{subject to} \quad & g(p, \theta, h) = 0 \text{ and } f(p, \theta, h) = 0 \\
& h(\vec{x}) > h_0 \\
& \text{for a given } \vec{V}, \mu, p_{\text{cav}}.
\end{aligned} \tag{7}
$$

where $h(\vec{x})$ is the generic gap height distribution and h_0 is the minimal gap height as shown in Fig. 1. The optimization is constrained by the fulfillment of a partial differential equation i.e. the Reynolds equation with cavitation, where p and θ are the unknowns and h is the optimization parameter. The objective is to find the values of the variable field $h(\vec{x})$ for all $\vec{x}$ which optimize an objective function of the form $f_{\text{obj}}(\bar{p}, \theta, h)$ under the constraint $g(\bar{p}, \theta, h) = 0$ and $f(\bar{p}, \theta, h) = 0$.

This class of optimization problems can be more conveniently rearranged as a minimization problem of a Lagrangian functional in the following form:

$$
\mathcal{L}(\bar{p}, \theta, \lambda_p, \lambda_\theta, h) = - f_{\text{obj}}(\bar{p}, \theta, h) \\
+ \int_{\Omega} \left(\lambda_p g(\theta, \theta, h) + \lambda_\theta f(\bar{p}, \theta, h) \right) d\Omega \tag{8}
$$

where $\lambda_p(\vec{x})$ is the adjoint pressure and $\lambda_\theta(\vec{x})$ the adjoint cavity fraction. Since the constraints $g(\bar{p}, \theta, h) = 0$ and $f(\bar{p}, \theta, h) = 0$ are always fulfilled, minimizing the objective function f_{obj} is equivalent to the minimization of the whole Lagrangian functional $\mathcal{L}(\bar{p}, \theta, \lambda_p, \lambda_\theta, h)$ in Eq. (8). Therefore, in the optimal point the gradient of the Lagrangian function is zero for all variables and we can derive the following three sets of equations:

$$
\left.
\begin{aligned}
\frac{\delta \mathcal{L}}{\delta \lambda_p} &\equiv g(\bar{p}, \theta, h) = 0 \\
\frac{\delta \mathcal{L}}{\delta \lambda_\theta} &\equiv f(\bar{p}, \theta, h) = 0
\end{aligned}
\right\}
\begin{aligned}
&\text{Reynolds equation} \\
&\text{with cavitation}
\end{aligned}
\tag{9}
$$

$$
\left.
\begin{aligned}
\frac{\delta \mathcal{L}}{\delta \bar{p}} &\equiv l_p(\bar{p}, \theta, \lambda_p, \lambda_\theta, h) = 0 \\
\frac{\delta \mathcal{L}}{\delta \theta} &\equiv l_\theta(\bar{p}, \theta, \lambda_p, \lambda_\theta, h) = 0
\end{aligned}
\right\}
\text{adjoint equation}
\tag{10}
$$

$$\frac{\delta \mathcal{L}}{\delta h} \equiv d(\bar{p}, \theta, \lambda_p, \lambda_\theta, h) = 0 \quad \text{decision equation.} \tag{11}$$

The solution of the three sets of equations will give the optimal film height $h(\vec{x})$ with the corresponding pressure field $\bar{p}(\vec{x})$ and mass fraction $\theta(\vec{x})$, as well as the adjoint variable field $\lambda_p(\vec{x})$ and $\lambda_\theta(\vec{x})$. Eq. (9) represents the already shown Reynolds equation and the complementarity equation, while Eq. (10) is the set of adjoint equations which reads:

$$
\begin{cases}
\nabla \cdot \left(-\frac{h^3}{12\mu} \nabla \lambda_p \right) + \left(1 - \frac{p}{\sqrt{p^2 + \theta^2}} \right) \lambda_\theta = \frac{\partial f_{\text{obj}}}{\partial \bar{p}} \\
\nabla \cdot \left(\frac{1}{2} h \vec{V} \lambda_p \right) + \left(1 - \frac{\theta}{\sqrt{p^2 + \theta^2}} \right) \lambda_\theta = 0.
\end{cases}
\tag{12}
$$

Its boundary conditions are assigned in the same manner as for the Reynolds equation with cavitation, i.e. by assigning the value of the multipliers on Σ_D and the flux of the multipliers on Σ_N. The know term of the second line of Eq. (12) is zero since the objective function f_{obj} does not depend on the cavity fraction θ. Further details of Eq. (12) are given in appendix.

The third Eq. (11) is called decision equation which relates the direct variable and the adjoint variable to the variation of the gap height $\bar{h}$ which minimizes the objective function. At this point one could follow two different strategies for the implementation of the optimization algorithm according to the derivation of the decision equation.

The first strategy consists of the derivation of the Lagrangian formulation with the objective function expressed in Eq. (7). Since the objective function does not depend on the gap height, one can directly compute the decision equation (11) in the following way:

$$d(\bar{p}, \theta, \lambda_p, \lambda_\theta, h) = -\frac{3h^2}{12\mu} \nabla \lambda_p \cdot \nabla p + \frac{1}{2} \nabla \lambda_p \cdot \vec{V} (1 - \theta) = 0. \tag{13}$$

The influence of the Lagrangian multiplier of the cavity fraction λ_θ is not considered since the complementarity equation (4) does not depend on the gap height h. Eq. (13) is an algebraic equation which introduces the concept of sensitivity, i.e. the direct influence of the design parameter h on the objective function f_{obj}:

$$S(\vec{x}) \equiv \frac{d f_{\text{obj}}}{d h} = -\frac{3h^2}{12\mu} \nabla \lambda_p \cdot \nabla p + \frac{1}{2} \nabla \lambda_p \cdot \vec{V} (1 - \theta). \tag{14}$$

where $S(\vec{x})$ is the sensitivity [25,42]. It is then clear that an iterative approach to the optimization problem can be pursued by updating the geometry by a quantity which is proportional to the sensitivity:

$$h^{n+1}(\vec{x}) = h^n(\vec{x}) + \varepsilon S^n(\vec{x}) \tag{15}$$

where ε is an under-relaxation coefficient determined empirically in order to ensure a fast convergence rate without instabilities.

It should be noted that a smoothing process is required after every update in order to increase the stability and prevent sharp edges in the solution which could lead to unrealistic shapes. This has been realized through a Gaussian filter as proposed by Bletzinger [43] and Stück and Rung [44] by applying a Gaussian smoothing in the following form:

$$h_s(\vec{x}) = F_s h(\vec{x}) = \int_{\Omega} K(\vec{r}; \sigma) h(\vec{x} - \vec{r}) d\vec{r}, \quad \forall \vec{x} \in \Omega \tag{16}$$

where h_s is the smoothed gap height, h is the updated gap height from Eq. (15), F_s is the filtering operator, $\vec{r}$ represents the local filter radius and σ is the standard deviation of the Gaussian filter kernel K. In this work σ is also referred to as the amplitude of the smoothing. The filter operator K is normalized so that:

$$\int_{\Omega} K(\vec{r}; \sigma) d\vec{r} = 1 \quad \forall \vec{x} \in \Omega. \tag{17}$$
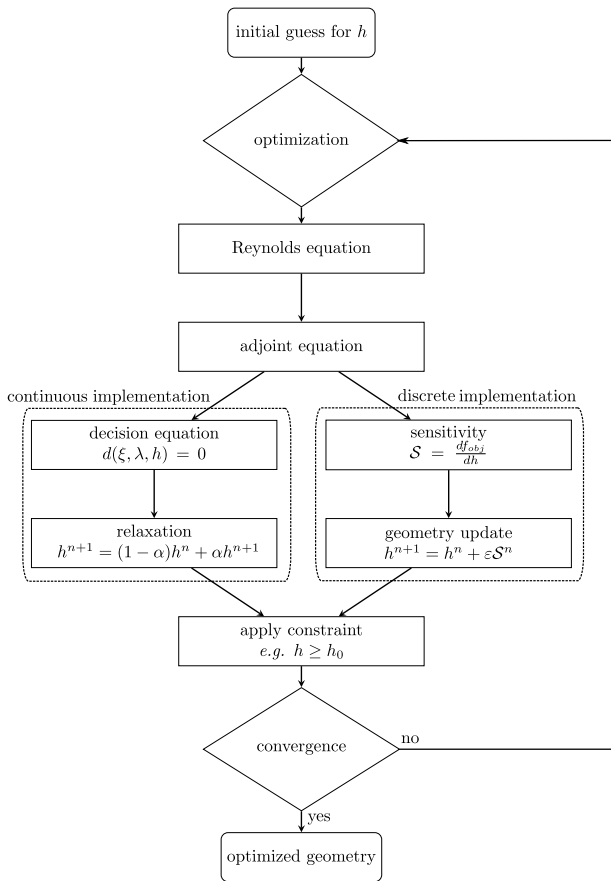
Fig. 2. Flowchart of the optimization process. The computation of the sensitivity and of the update of the gap height are presented for both the continuous as well as the discrete implementation.

In this way the integral of the shape is not altered, while fine scale oscillations due to the derivative computation are damped [44]. The filter is applied after updating the geometry in Eq. (15) and before applying the eventual constraints.

Such an iterative approach is also used, for example, in aeronautics for shape optimizations under the constraint of the Navier–Stokes equation [28]. This first optimization strategy has been implemented in Matlab® through a finite volume scheme and its detailed are shown in Appendix. The corresponding optimization process is shown in the right branch of the flowchart in Fig. 2.

The second method to implement the optimization strategy employs a smoothing term directly in the objective function. This way the optimizer will find the equilibrium between the maximization of the load carrying capacity and a certain smoothing hence avoiding unfeasible shapes. This implementation was first presented by Van Ostayen for the optimization of dynamically loaded bearings in the hydrodynamic regime [32]. The smoothing term is introduced by modifying the objective function in the following way:

$$f_{\text{obj}} = -W + \frac{1}{2}\epsilon\delta x \int_{\Omega} (\nabla \bar{h})^2 d\Omega \qquad (18)$$

where ϵ represents the smoothing amplitude, δx is the local mesh size and $\bar{h} = h - h_0$ is the geometry update as shown in Fig. 1. This way, the decision equation (11) includes now the Laplacian of the update of the gap height as additional term:

$$d(\bar{p}, \theta, \lambda_p, \lambda_\theta, h) = \nabla \cdot \left(\epsilon\delta x \nabla \bar{h}\right) - \frac{3h^2}{12\mu}\nabla\lambda_p \cdot \nabla p \qquad (19)$$
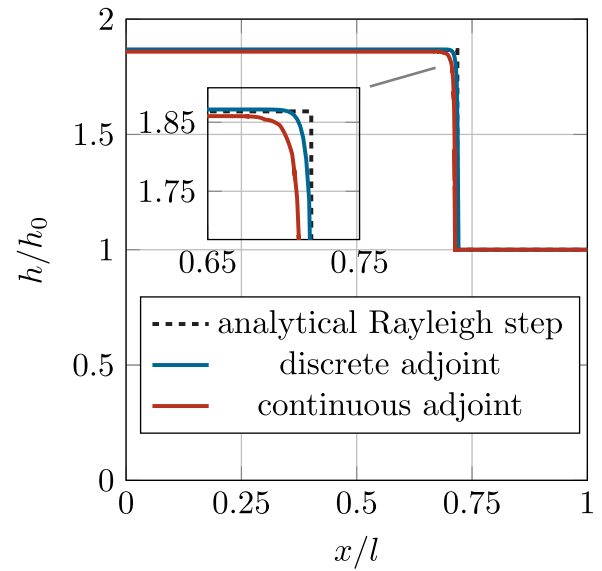$$+ \frac{1}{2}\nabla\lambda_p \cdot \vec{V}(1-\theta).$$

Fig. 3. Validation of the adjoint implementation with analytical and direct methods. Comparison between the analytical solution of the 1D Rayleigh step and the solution of the discrete and continuous adjoint method. The curves are non dimensionalized. The inlet pressure is set equal to the outlet one.

This partial differential equation can be solved for $\bar{h}$ with natural boundary conditions. The implementation of this second strategy follows the path shown in the left branch of the flowchart in Fig. 2.

The second strategy presents some practical aspects from the computational point of view since the simultaneous solution of the three partial differential equations (Eqs. (9), (10), (11)) can be efficiently implemented in commercial finite element software such as Comsol® [33]. This approach is also referred to as the one-shot approach since the solver minimizes the Lagrangian formulation by setting its total gradient to zero, as shown by Slawig in [45].

Both the Comsol® and the Matlab® implementations also represent the two typical ways of addressing the adjoint method, namely the continuous and the discrete adjoint method respectively. In the continuous adjoint method the three Eqs. (9), (10) and (19) are first analytically derived and then discretized. In turn, the discrete method exploits the discretized form in order to build the solving system for the adjoint equation (10) and finally solves the decision equation in its algebraic form (14). A detailed derivation of the discrete adjoint method is given in Appendix.

A quantitative comparison of the performance of the two approaches has been performed by Nadarajah and Jamson for the adjoint optimization constrained by the Navier–Stokes equation [46]. They show that the two approaches converge to the same solution for a sufficiently fine mesh with minor differences at the boundaries where the discrete method shows a better convergence despite its slightly higher computational requirements. The two different implementations of the optimization scheme for the present work are validated and compared quantitatively against each other in Section 3.

3. Validation

Due to the novelty of the proposed optimization method, we present a validation of both implementations of the adjoint method in this section. A typical textbook example of an optimization problem for lubricant thin films is the 1D Rayleigh step which maximizes the load carry capacity of a 1D slider bearing. Fig. 3 shows the comparison between the analytical curve and the two optimal solutions with the continuous and discrete adjoint method. As one can see the analytical shape is fully recovered by both methods, showing an inlet to outlet
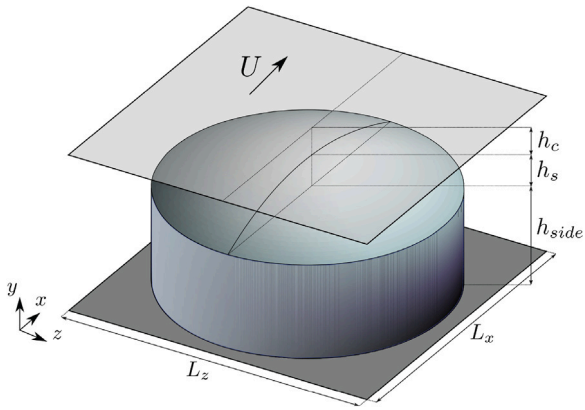
Fig. 4. Schematic representation of the pin geometry in a pin-on-disc tribometer. The pin has a parabolic profile whose height at the center is h_s, while the minimum gap height at the center of the geometry is h_c. The side of the pin h_{side} is 1 mm high. The domain is size is L_x and L_z in the x- and z-direction respectively.
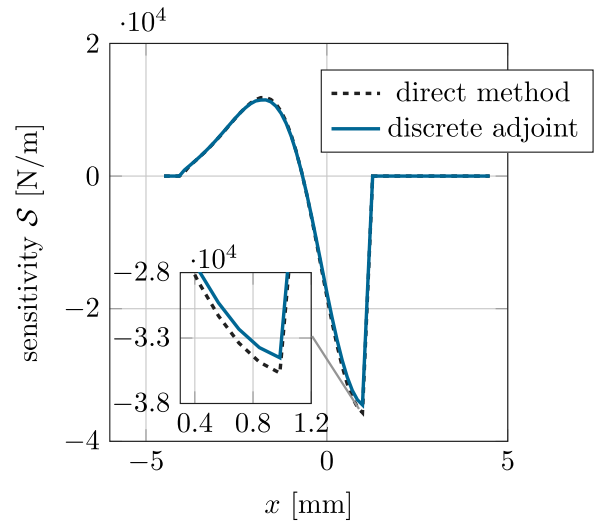

Fig. 5. Validation of the adjoint implementation with analytical and direct methods. Sensitivity in the centerline at the first iteration step for the pin with parabolic shape. The sensitivity is shown with its dimensional value [N/m] since it relates the variation of the normal force (object function) to a variation in the geometry.

Table 1
Simulation parameters used in the results section.

h_c	1 μm
h_s	1 μm
h_{side}	1 mm
$L_x = L_z$	9 mm
R_{pin}	4 mm
μ	0.01 Pa·s
U	0.1 m/s
P_{amb}	101325 Pa
P_{cav}	80000 Pa

ratio of 1.86 and a normalized step position at 72% of the bearing length [2]. In both optimization strategies the minimal film height was constrained to be equal to 1.0. If left unconstrained, the optimizer would reduce the film height towards zero in order to obtain the maximum load.

With respect to the 2D Rayleigh step without cavitation, Van Ostayen presented the optimized shape in [32] showing a very good agreement in terms of non dimensional load carrying capacity with the optimized solution of Rhode [32].

Cavitation does not occur in the optimal 1D Rayleigh step solution. In order to check the optimization methods in a cavitated lubricating film, we performed a further comparison with a more complicated geometry, namely a pin-on-disc tribometer. The pin used for this comparison has a circular base and a parabolic profile as shown in Fig. 4. The chosen dimensions of the pin match those used in the experimental campaign by Braun et al. [34], where a radius $R_{pin} = 4$ mm was chosen, while the parabolic profile of the pin surface has a shoulder height of 1 μm. The discrete method uses a uniform mesh consisting of 1025x1025 grid points corresponding to a mesh size of 8.78 μm. Further information about the mesh convergence are given in Ref. [14]. There is no analytical solution available for the comparison of such a geometry in presence of cavitation, but it is possible to validate the first step of the optimization loop through a comparison with a direct method to compute the sensitivity. In the direct method the total derivative of the Lagrangian formulation in Eq. (8) with respect to the design parameter can be obtained by introducing a Dirac delta perturbation $\delta h(\vec{x})$ in the reference geometry and measuring the effect of it on the objective function directly. This way, the sensitivity can be computed in the following way:

$$S(\vec{x}) = \frac{d f_{obj}}{d h} = \frac{W_{\delta h(\vec{x})} - W_{ref}}{\delta h(\vec{x})} \tag{20}$$

where $W_{\delta h}$ is the load computed with the perturbed geometry and W_{ref} is the reference load.

Fig. 5 shows the sensitivity evaluated in the centerline of the pin with both the direct method and the discrete adjoint method at the first step of the optimization loop, when the geometry is still the reference one. As on can see, the two curves are in close agreement. The sensitivity is defined such that a positive value of it means that the gap height should be increased while a negative value implies a reduction of the gap height. Moreover, it is interesting to notice that the second part of the pin surface, where the sensitivity is zero, corresponds to the cavitation region. This hints to the fact that there is no advantage to modify the surface in the cavitation region.

The simple geometry of the parabolic pin also allows comparing the continuous and discrete adjoint results. For this comparison the same uniform mesh is used for discrete method as for the sensitivity computation shown in Fig. 5. On the other side, the COMSOL implementation of the continuous method employs a triangular mesh with a typical element size of 8 μm.

This is shown in Figs. 6(a) and 6(b) where the optimized geometry and its corresponding pressure profile are shown for both the adjoint methods and the reference case. The continuous and the discrete method are overall in good agreement. The small differences in the corners of the two optimal solutions are due to the different smoothing procedures as explained in Section 2.

4. Results and discussion

In this section we apply the optimization through the adjoint method to a pin-on-disc tribometer. Similar optimization attempts documented in the literature treat cases without cavitation [5,6,32]. This specific experimental device is chosen since it is representative for typical tribological applications in which cavitation occurs. Moreover, pin-on-disc tribometers are widely used for testing texture designs, hence easing the eventual experimental validation of the optimization results presented here.

Fig. 4 shows the reference geometry of the pin of a pin-on-disc tribometer. The surface has a parabolic profile in order to model the rounding effects on the edge of the pellet which are typically created by the manufacturing processes such as polishing and grinding. Geometrical and operating parameters are presented in Table 1. Although our COMSOL implementation of the adjoint method (continuous) is
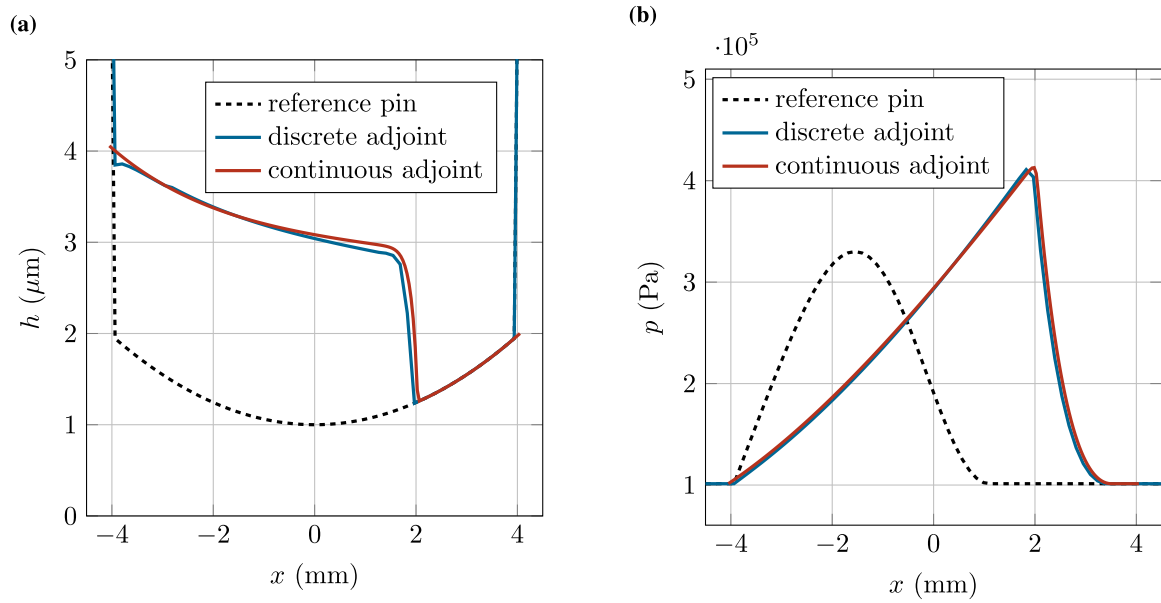
(a)

(b)

Fig. 6. Validation of the discrete and continuous adjoint implementations with the geometry of the parabolic pin in presence of cavitation. a, Comparison between the continuous and the discrete adjoint methods for pin with parabolic shape. The parabola is 1 μm high as well as the gap height at the center. b, Comparison of the pressure profile in the centerline of the pin. The comparison is carried out with the following operating parameters for both figures: $U = 0.1$ m/s, $\mu = 0.0028$ Pa·s, $P_{cav} = P_{in} = 101325$ Pa.

computationally faster than the MATLAB one (discrete), the results in this section are computed only by using the discrete adjoint method out of practical reasons in the data management.

4.1. Sensitivity

One of the first relevant insights that we can deduce from the adjoint method is the sensitivity map of the surface, or, in other words, the direct influence of a gap height modification on the load carrying capacity as presented in Eq. (14). Fig. 7(a) shows the sensitivity of the reference pin geometry and Fig. 7(b) shows the corresponding pressure distribution. The sensitivity is computed by evaluating the algebraic sensitivity equation (14) for the initial geometry shown in Fig. 4. As one can see three regions can be clearly identified. The first region covers the front part of the pin and is characterized by a positive value of the sensitivity. This means that in this region an increase of the gap height leads to an increase of the normal force. This is, therefore, the part of the pin surface which should be textured in order to achieve a higher load carrying capacity. It is also important to notice that any addition on top of the pin surface, i.e. a reduction of the film height, would decrease the load carrying capacity, hence asperities elements [47] should not be added here.

In the second region the sensitivity is negative, meaning that a reduction of the gap height would be beneficial for the load carrying capacity. At this point it is up to the designer to choose if the surface can be manipulated in both directions or eventually only in one (*i.e.* if the gap height h can be increased or decreased). In the present work we focus only on surface modifications which are based on texturing techniques, hence allowing the surface to be modified only inwards *e.g.* by etching or by laser texturing. This is done by setting the additional constraint that the optimized gap height $\bar{h}$ can be only bigger than the reference one:

$$\bar{h}(\vec{x}) > h_{\text{ref}}(\vec{x}). \tag{21}$$

The last region of the sensitivity concerns the part of the domain where cavitation occurs. In this region the sensitivity is zero, meaning that any geometry modification would have no consequences on the load carrying capacity (as long as it remains under a certain amplitude). This has been already shown in literature, for example by Gercha et al.

who studied surface textures in a parallel bearing and showed how the texture had no impact if the whole fluid film is cavitated [48]. The same conclusion is reached in the work of Codrignani et al. [14] who investigated the effects of a single dimple on a pin in a manner similar to the direct method shown in Section 3.

We note that during the optimization process the size and the position of the three regions may change. It could therefore become beneficial to place texture elements in region with initial negative sensitivity after some iterations of the optimizer.

4.2. 2D Rayleigh step

Fig. 8(a) shows the pin geometry after convergence of the optimizer, hence until the relative residual of the gap height distribution r_h^n:

$$r_h^n = \int_\Omega \frac{|h^n(\vec{x}) - h^{n-1}(\vec{x})|}{|h^{n-1}(\vec{x})|} d\Omega \tag{22}$$

drops below 10^{-5}. The optimized surface consists of a single big pocket in the front part of the pin, the geometry of a 2D Rayleigh step. A similar geometry is typically analyzed in the literature for slider bearings, as described, among others, by Rohde [5], Shen & Khonsari [6] and Fillon & Dobrica [18].

Thanks to the optimization the pin almost doubled its load carrying capacity, going from a normal force of $F_N = 8.64$ N to 16.79 N. This is revealed by Fig. 9, that shows the convergence of both the normal force and the friction coefficient over the optimization steps. The final pressure distribution is shown in Fig. 8(b), with a maximum pressure of around 1.4 MPa while the unoptimized Rayleigh step yields 0.9 MPa. The adjoint formulation applied in this work assures that the normal force corresponds to the maximum, while, on the other side, it cannot be proven *a priori* that the friction coefficient is globally minimized. Nonetheless, as already stated in Section 2, an increase in the load carrying capacity leads to an increase of the gap height which, in turn, corresponds to a friction reduction. Furthermore, optimizing the load carrying capacity and therefore increasing the fly height for a given load, will result in an earlier transition from mixed lubrication to hydrodynamic lubrication.

The discrete optimizer reached convergence after 1000 iterations which is as computationally expensive as running 2000 simulations of
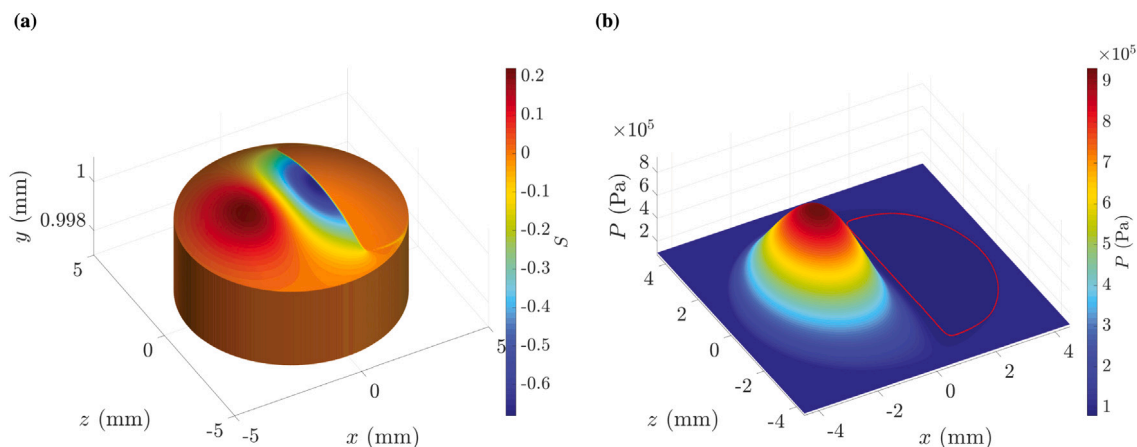
(a) **(b)**

Fig. 7. Analysis of the reference untextured pin. a, Sensitivity over the pin geometry at the first optimization step. A positive sensitivity implies that the gap height should be increased in order to achieve a higher load carrying capacity. The vertical y axis is 1000 magnified in comparison to the other two ones. b, Pressure distribution of the parabolic pin. The cavitation region is delimited by a red line. The lubricant fluid flows from left to right in the x direction. (For interpretation of the references to color in this figure legend, the reader is referred to the web version of this article.)
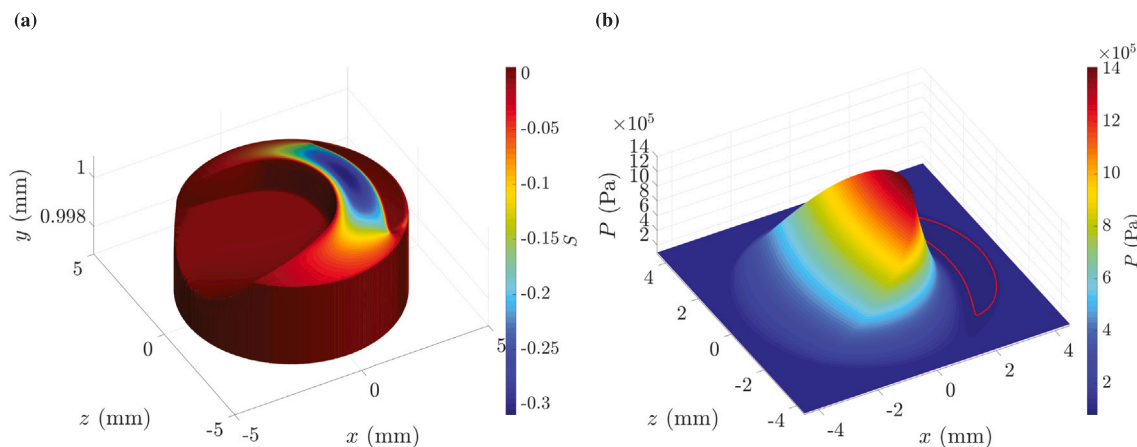
(a) **(b)**

Fig. 8. Optimized pin geometry and pressure distribution with the 2D Rayleigh step. The optimization has the only constraint that the gap height cannot be reduced as stated in Eq. (21). a, Geometry of the optimized 2D Rayleigh step. The sensitivity is plotted over the surface of the pin. The vertical y axis is 1000 magnified in comparison to the other two ones. b, Pressure distribution over the optimized 2D Rayleigh step. The cavitation region is delimited by a red line. The lubricant fluid flows from left to right in the x direction. (For interpretation of the references to color in this figure legend, the reader is referred to the web version of this article.)
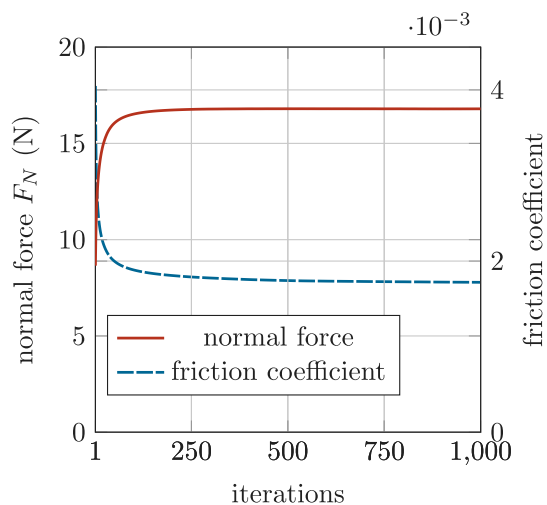

Fig. 9. Convergence of the normal force and of the friction coefficient during the optimization iterations. The simulations are stopped as soon as the residual on the gap height variation $\bar{h}$ drops below 10^{-5}.

the Reynolds equation, since each step consists of the solution of the Reynolds equation and the adjoint one. For the same level of accuracy, this is faster than describing the Rayleigh step geometry through a parametric study, since we are optimizing the geometry point by point. In particular, the resolution of the system with a grid of 1025x1025 points took 10 h on a single core of a laptop. The iteration number can be consistently reduced by solving the Eqs. (9), (10) and (11) in a single system, as presented in Section 2 for the COMSOL implementation of the continuous adjoint method.

As a next step we would like to consider more complex constraints and their impact on the optimal solution. In particular the geometry of the 2D Rayleigh step could introduce some experimental challenges if tested on a pin-on-disc tribometer because of its behavior in the mixed lubrication region where contact could occur on the sharp edges of the Rayleigh step. In order to avoid this effect we add a further constraint which will force the initial contact to occur in the central part of the pin. This can be done, for example, as shown in Fig. 10 where the central stripe along the centerline of the pin is constrained to remain untextured. The introduction of such a constraint reduces the improvement in the load carrying capacity. In particular the resulting normal force is $F_N = 14.42$ N which is just two thirds of the performance obtained with the full 2D Rayleigh step. As one can see from Fig. 10
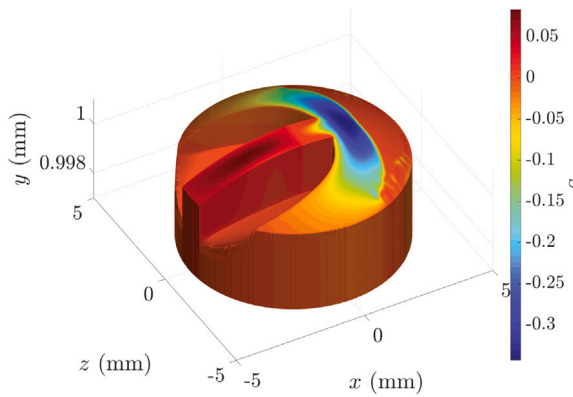
Fig. 10. Sensitivity over the optimized pin geometry with the additional constraint which eases the effective texturation on a real pin-on-disc tribometer. The central stripe has a width of 30% of the pin radius. The vertical y axis is 1000 magnified in comparison to the other two ones.

the sensitivity on the front part of the stripe is positive, meaning that the constraint prevents the increase of the gap height in a region where this would be beneficial for the load carrying capacity.

4.3. Optimization of surface textures

In order to apply the adjoint method to the optimization of surface textures we need to add two further constraints: the texture pattern and the size of each element. Among the numerous shapes that texture elements can have we focus here only on elements which have a circular base, where each grid point inside the texture element remains an optimization variable. The actual local depth of the optimal texture element will be automatically determined by the algorithm. The texture pattern is a pseudo-hexagonal one in which each texture element is equally spaced in both directions and each second row is shifted of half the distance in the z-direction as already used in [14].

Figs. 11(a) and 11(b) show the optimized textured surface and the corresponding pressure distribution for a pseudo-hexagonal pattern made by circular dimples with a diameter $D = 200$ μm. As we can see the texture elements in the part of the domain with positive sensitivity were automatically selected to increase in depth. This is one of the biggest advantages of the adjoint method, because usual parametric techniques place texture elements also in region where their presence is detrimental [4]. Moreover, the gap height distribution inside the texture elements is optimized point by point, meaning that also non circular shapes may be found. This can be seen in the elements on the lateral side of the pin which assume a rather elongated shape. This shape helps the lubricant flow to reach the central part of the pin in order to enhance the load carrying capacity by bringing more fluid where the gap height is lower. This could also explain why some elements between the fully circular ones and the elongated ones have a barrier inside them which splits the elements in two. All texture elements in this case have rather sharp edges because of the low amplitude of the smoothing $\sigma = 0.3$ applied at each iteration step.

By increasing the smoothing amplitude to $\sigma = 1.2$ the shapes of the texture elements become more uniform as one can see in Fig. 12(a). Nonetheless the elements on the side still assume an elongated form. The smoothing has hence a non negligible impact on the optimal solution and thus on the value of the load carrying capacity. In fact the normal force of the slightly smoothed case is $F_N = 9.1823$ N while the heavily smoothed case delivers a lower force $F_N = 9.0623$ N. Even though both cases yield an increase of the load carrying capacity, it is clear that an excessive smoothing could harm the optimal performance, as reported also for other works on the adjoint optimization [44].

The difference between the two values of the smoothing amplitude can be seen in Fig. 12(b) where the profile at the centerline of the pin is shown for both cases. The less smoothed elements exhibits sharper edges which resemble those of a cylindrical dimple while the smoothed and less effective dimples have a shape similar to a spherical one. This aspect should be considered in experimental activities because laser surface texturing is unable to create very sharp edges. This finding is in agreement with the results of other works which investigated the texture shape though parametric studies, such as Aggarwal & Pandey [49], Adjemout et al. [35] and Nanbu et al. [50].

The spacing l_x and l_z between texture elements is chosen so that the texture density is $\rho_{\text{txt}} = 15\%$ if the whole pin surfaces is textured. In practice, since dimples appear only where $S > 0$, the overall texture density is lower. This hints at the fact that the definition of texture density ρ_{txt} should take into account the sensitivity analysis. In fact the optimal value of texture density is simply 100% of the region with positive sensitivity which corresponds to the 2D Rayleigh step shown in Fig. 8(a).

As final comment to this subsection we note that special care has to be taken in the analysis of the validity of optimized shape, since texture elements with an excessive depth-to-diameter ratio may violate the applicability assumption of the Reynolds equations as discussed by Dobrica and Fillon [51]. The optimized texture in this section has a maximal depth-to-diameter ratio of 1/200 which is way below the limit of 1/10 found in [51].

4.4. Comparison between different optimization techniques for surface textures

The great advantage of the adjoint method in comparison to typical parametric studies is its ability to optimize the whole surface point-by-point. In particular, in the case of surface textures, the shape of every single texture element can be optimized according to its position on the macro-geometry. In order to assess the effectiveness of this optimization technique a comparison is carried out between the optimized surface presented in the previous section and the results of the same kind of texture pattern which is optimized through a parametric study with spherical dimples.

Fig. 13 shows a comparison of the load carrying capacity with the untextured reference case of the different constraints seen in the previous section and also with three parametric studies. At first we focus on the impact of the constraints on the load carrying capacity by comparing the first five columns. As one can see the best increase of the normal force is obtained by the Rayleigh step (column b), hence by optimizing each point of the surface under the only constraint that the surface cannot be extruded Eq. (21). Column c concerns the case with an additional stripe in the middle of the pin (see Fig. 10) which acts as a further constraint which reduces the effectiveness of the Rayleigh step. Columns d and e represent the adjoint optimization of the surface texture presented in Section 4.3 which has texture elements arranged in a pseudo hexagonal pattern. As we can see the introduction of such an invasive constraint has lowered the increase of the normal force, showing that the Rayleigh step is the best way to increase the normal force in conformal contacts. Nonetheless columns d and e show a higher normal force than all the remaining columns which correspond to the parametric texture optimization. In particular we analyzed in this work two recurrent cases in literature, namely the presence of texture elements on the whole surface (last column) or only on the front part (second last column). Front textures are known to perform better than total ones and the reason can be clearly seen from the sensitivity distribution in Fig. 7(a) where the sensitivity in the rear part of the pin is either negative or zero. Therefore, we also consider the case in which the parametric optimization is carried out by placing texture elements only in regions of positive sensitivity, see Fig. 7(a). The normal force of this case is shown in the third last column where we can observe that thanks to the additional information provided by the computation of
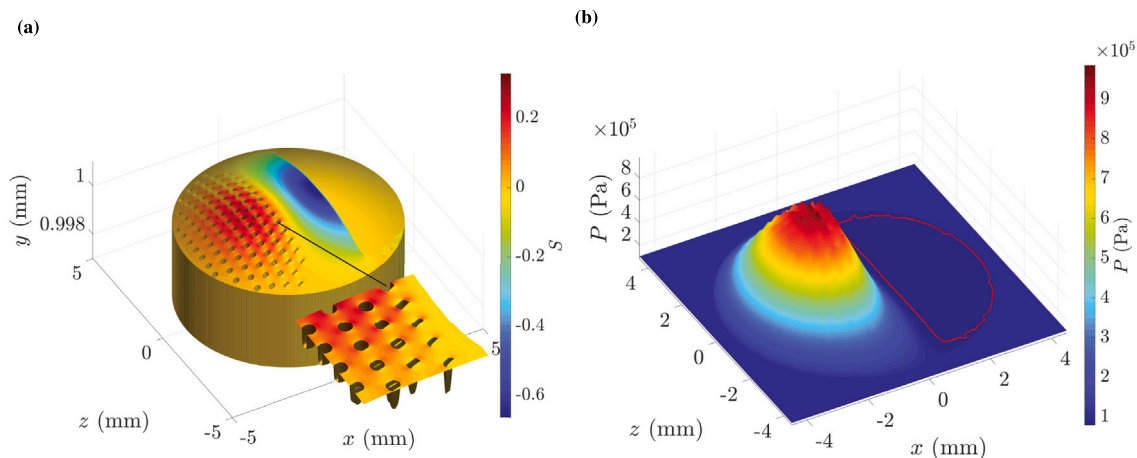
(a)   **(b)**

Fig. 11. Optimization of texture on the pin surface. The texture has a pseudo-hexagonal pattern and the dimples are constrained to have a maximal diameter $D = 200$ μm. a, Sensitivity over the textured pin surface with low smoothing amplitude $\sigma = 0.3$. The vertical y axis is 1000 magnified in comparison to the other two ones. b, Pressure distribution. The cavitation region is delimited by a red line. (For interpretation of the references to color in this figure legend, the reader is referred to the web version of this article.)
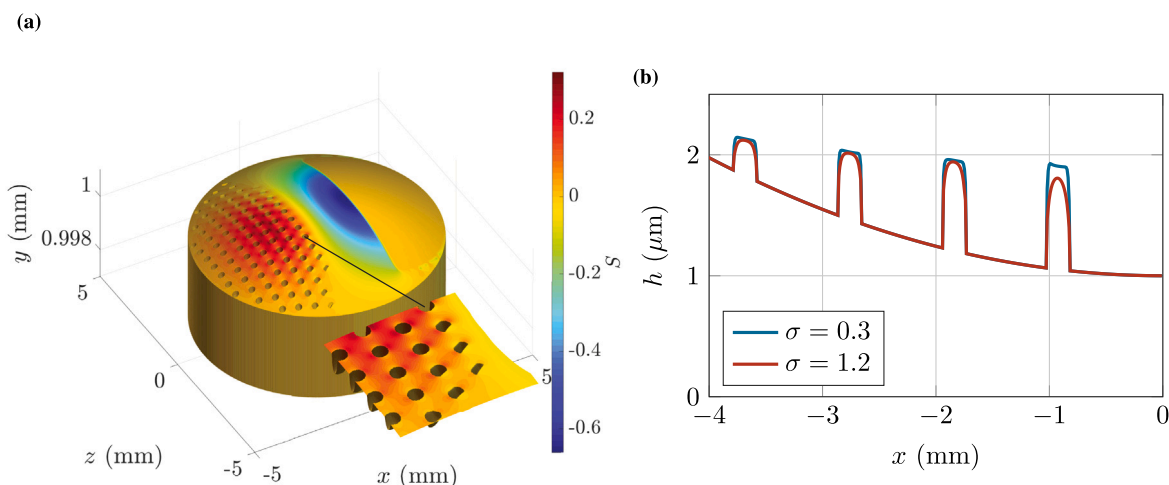
(a)   **(b)**

Fig. 12. Analysis of the impact of the smoothing amplitude σ. a, Sensitivity over the pin geometry. With high smoothing amplitude $\sigma = 1.2$. The vertical y axis is 1000 magnified in comparison to the other two ones. b, Comparison of the centerline gap height for different values of smoothing amplitude σ. The gap height is 1000 magnified in comparison to length of the pin.

the sensitivity, this case is the best among the parametrically optimized ones. However, the texture optimized with the adjoint method performs better since it can find the optimal shape and depth of every texture element according to their position on the surface.

It is important to notice that, for the chosen operating parameters and geometry, the absolute improvement in load carrying capacity is small (< 7%) with every optimization techniques shown in Fig. 13. This could be due to the fact that the simulations are carried out in the hydrodynamic regime. An higher impact of the texture may be encountered in the mixed lubrication regime, as found both experimentally and numerically in previous works [34,52,53].

As final remark for this section we would like to underline that, although the practical realization of textures with different element size may result challenging [54,55], a great improvement can be still achieved through the sensitivity analysis and assuming a constant shape for each texture element as shown in Fig. 13 column f.

4.5. Generalization of the optimized geometry for different operating conditions

As seen in the previous subsection, the adjoint method finds optimal texture elements which have different shape and depth according to

their position on the macro geometry. Nonetheless some characteristics of the optimized texture can be generalized as function of the operating conditions so that some general design rules can be defined. This can be done for example by analyzing the average depth of the texture elements as a function of the gap height for different combinations of viscosity and velocity as shown in Fig. 14. The dynamic viscosity is varied in the range $0.0028 < \mu < 0.28$ Pa·s while the wall velocity ranges between 0.01 and 1 m/s. The simulations are carried at imposed gap height from 0.5 to 10 μm. This results in a variation of the Sommerfeld number based on the gap height between $0.092 \cdot 10^6$ and $8.49 \cdot 10^6$. As one can see the optimal depth varies linearly with the gap height. This linear behavior has been found also by parametric studies in literature [8,14,53]. Nonetheless, the particularity of the adjoint method is that the texture elements appear only where the sensitivity is positive, hence avoiding to have texture elements which actually have a detrimental effects on the load carrying capacity.

5. Conclusion

We present for the first time the implementation of the adjoint method for the optimization of surface textures in hydrodynamically lubricated contacts with cavitation and its validation. This method
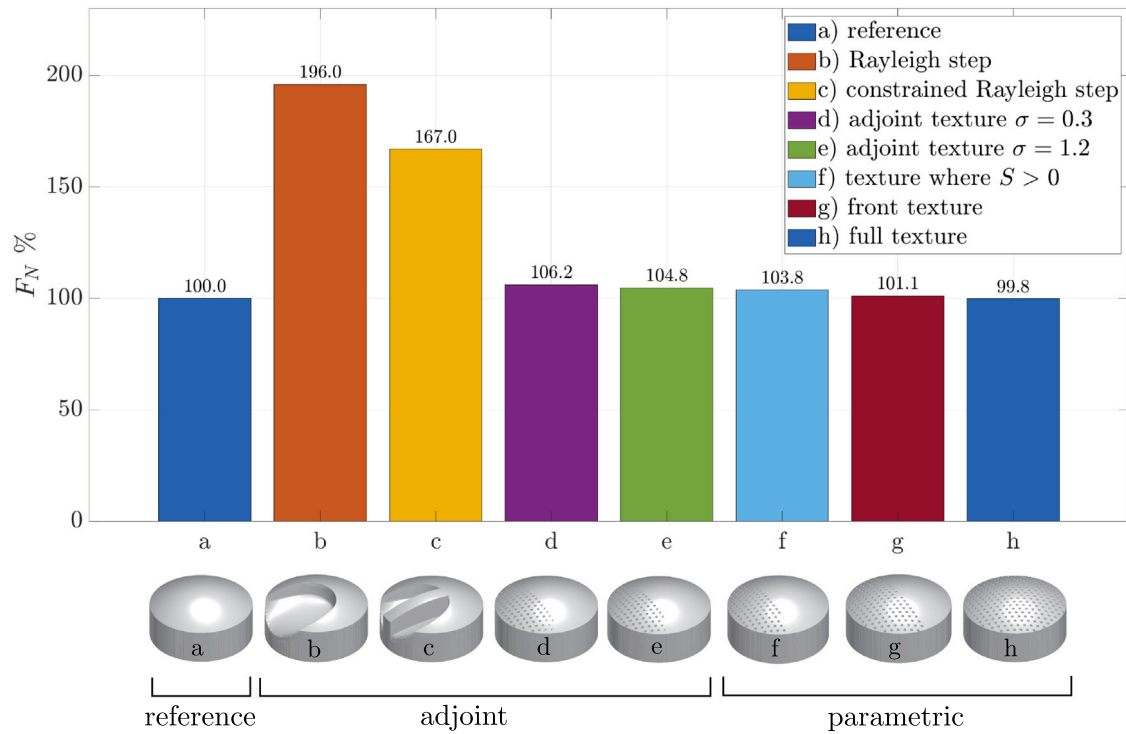
Fig. 13. Performance of the adjoint optimization for different constraints. The figure shows also the comparison with parametric studies for textured surfaces done in this work. The normal force is displayed as percentage of the untextured case a. The operating parameters of this comparison are reported in Table 1.
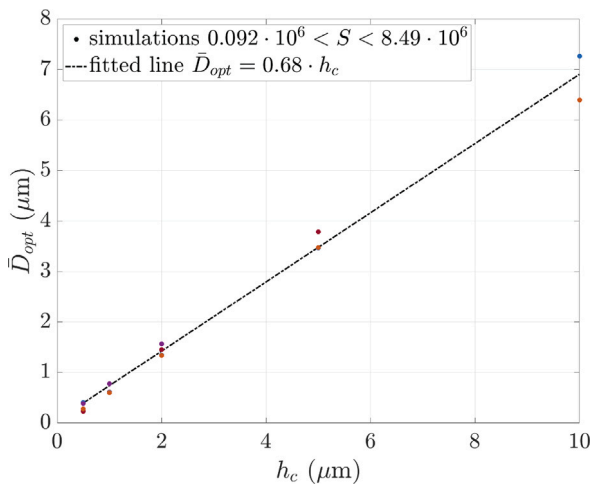

Fig. 14. Average dimple depth as function of the gap height. Each point represent a different combinations of velocity and viscosity so that the following range of Sommerfeld number is swept: $0.092 \cdot 10^6 < S < 8.49 \cdot 10^6$. The simulations are carried out at constant gap height.

allows to fine-tune each single texture element individually rather than through a trial and error approach with dimples of identical geometry. The adjoint method is more effective than traditional parametric approaches for the optimization of the texture shape. This is because it can determine where textures should be and how the texture shape should look like in a single simulation without the need to parametrize the texture with elementary shapes. This allows to carry out free-form optimizations in a computationally efficient manner.

We find that the traditional approach to texture the full front of the pin does not lead to an ideal increase in load carrying capacity. The sensitivity analysis reveals that it is beneficial to texture only part of the front portion of the pin. We carried out these optimizations as a function of operating conditions, confirming a linear relationship between the gap height and optimal texture depth. Further development of this work should include also thermal effects and the elasticity of the contact surfaces [56–59].

Declaration of competing interest

The authors declare that they have no known competing financial interests or personal relationships that could have appeared to influence the work reported in this paper.

CRediT authorship contribution statement

A. Codrignani: Conceptualization, Methodology, Software, Investigation, Data curation, Writing - original draft. **D. Savio:** Methodology, Writing - review & editing. **L. Pastewka:** Formal analysis, Writing - review & editing. **B. Frohnapfel:** Writing - review & editing. **R. van Ostayen:** Software, Validation, Visualization, Writing - review & editing, Supervision.

Appendix. Derivation of the discrete adjoint method

In this appendix we show the detailed derivation of the discrete adjoint method for the Reynolds equation with mass-conserving cavitation. The Reynolds equation (1) can be written in its linear formulation with the discretized unknown **p** and θ:

$$\mathbf{g} = \mathbf{Ap} + \mathbf{B}\theta - \mathbf{c} = 0 \tag{23}$$

where **g** is a vector containing the residuum of the Reynolds equation. The discretization is performed with the finite volume method [60]. The complementarity constraint in Eq. (4) is discretized by defining its residuum **f** in the following way:

$$\mathbf{f} = \bar{\mathbf{p}} + \theta - \sqrt{\bar{\mathbf{p}}^2 + \theta^2} = 0. \tag{24}$$

The nonlinear system can be solved with the Newton–Raphson method and its corresponding Jacobian matrix can be written in the following way [36]:

$$\mathbf{J} \begin{pmatrix} \delta p \\ \delta \theta \end{pmatrix} = \begin{bmatrix} \mathbf{J}_{\mathbf{f},p} & \mathbf{J}_{\mathbf{f},\theta} \\ \mathbf{J}_{\mathbf{g},p} & \mathbf{J}_{\mathbf{g},\theta} \end{bmatrix} \begin{pmatrix} \delta \bar{p} \\ \delta \theta \end{pmatrix} = - \begin{pmatrix} \mathbf{f} \\ \mathbf{g} \end{pmatrix}. \tag{25}$$

The computation of the Jacobian matrix is eased by the fact that its submatrices are already known from the discretization of the Reynolds equation (*e.g.* $\mathbf{J}_{\mathbf{g},\mathbf{p}} = \mathbf{A}$).

After having discretized the direct problem we can rewrite the Lagrangian formulation in its discrete formulation:

$$\mathcal{L} = -f_{\text{obj}} + \lambda_p^T \mathbf{g} + \lambda_\theta^T \mathbf{f} \tag{26}$$

where λ_p and λ_θ are vectors of Lagrangian multipliers. Since g and f are zero everywhere by definition, one can choose λ_p and λ_θ freely so that $\mathcal{L} = -f_{\text{obj}}$. This allows us to rewrite the sensitivity as

$$S \equiv \frac{df_{\text{obj}}}{dh} = \frac{d\mathcal{L}}{dh} = \left(-\frac{\partial f_{\text{obj}}}{\partial \bar{p}} + \lambda_p^T \frac{\partial \mathbf{g}}{\partial \bar{p}} + \lambda_\theta^T \frac{\partial \mathbf{f}}{\partial \bar{p}} \right) \frac{d\bar{p}}{dh}$$
$$+ \left(-\frac{\partial f_{\text{obj}}}{\partial \theta} + \lambda_p^T \frac{\partial \mathbf{g}}{\partial \theta} + \lambda_\theta^T \frac{\partial \mathbf{f}}{\partial \theta} \right) \frac{d\theta}{dh} \tag{27}$$
$$+ \lambda_p^T \frac{\partial \mathbf{g}}{\partial h} + \lambda_\theta^T \frac{\partial \mathbf{f}}{\partial h}.$$

By setting the two terms in the brackets on the right hand side to zero we obtain the system of the adjoint equations:

$$\begin{bmatrix} \frac{\partial \mathbf{g}}{\partial \bar{p}} & \frac{\partial \mathbf{f}}{\partial \bar{p}} \\ \frac{\partial \mathbf{g}}{\partial \theta} & \frac{\partial \mathbf{f}}{\partial \theta} \end{bmatrix} \begin{pmatrix} \lambda_p \\ \lambda_\theta \end{pmatrix} = \begin{pmatrix} \frac{\partial f_{\text{obj}}}{\partial \bar{p}} \\ \mathbf{0} \end{pmatrix} \tag{28}$$

where the term $\frac{\partial f_{\text{obj}}}{\partial \theta}$ is set to zero since the objective function does not depend on the gap height. The remaining right hand side term $\frac{\partial f_{\text{obj}}}{\partial \bar{p}}$ can be easily computed from the analytical definition of normal force in Eq. (5):

$$\frac{\partial f_{\text{obj}}}{\partial p} = \frac{\partial W}{\partial p} = \frac{\partial}{\partial p} \int_\Omega (p - p_{\text{ext}}) \, d\Omega = \int_\Omega 1 \, d\Omega. \tag{29}$$

Therefore $\frac{\partial f_{\text{obj}}}{\partial \bar{p}}$ is a 1D array which contains the area of the each single cell $d\Omega$. Eq. (28) is a linear algebraic equation whose solution can be obtained per substitution after having preconditioned the system in a similar manner as presented by Wolozynski et al. [36] for the cavitation algorithm.

The next step is to compute the sensitivity by solving the algebraic equation (27) which now reduces to:

$$S = \lambda_p^T \frac{\partial \mathbf{g}}{\partial h} \tag{30}$$

since the term $\lambda_\theta^T \frac{\partial f}{\partial h}$ is zero because the complementarity constraint does not depend on the gap height. In order to compute the sensitivity we first compute the analytical derivative of the Reynolds equation with respect to the gap height, *i.d.* the term $\frac{\partial g}{\partial h}$:

$$\frac{\partial \mathbf{g}}{\partial h} = \frac{\partial \mathbf{A}}{\partial h} \bar{p} + \frac{\partial \mathbf{B}}{\partial h} \theta \tag{31}$$

where $\frac{\partial \mathbf{A}}{\partial h}$ and $\frac{\partial \mathbf{B}}{\partial h}$ can be easily obtained from the implementation of the Reynolds equation (23).

The optimization can be now performed in an iterative way as explained in the flowchart in Fig. 2 in Section 2.

References

[1] Rayleigh Lord. I. Notes on the theory of lubrication. Lond Edinb Dublin Philos Mag J Sci 1918;35(205):1–12.

[2] Hamrock BJ, Schmid SR, Jacobson BO. Fundamentals of fluid film lubrication. CRC press; 2004.

[3] Etsion I. State of the art in laser surface texturing. J Tribol 2005;127(1):248–53.

[4] Gropper D, Wang L, Harvey TJ. Hydrodynamic lubrication of textured surfaces: A review of modeling techniques and key findings. Tribol Int 2016;94:509–29.

[5] Rohde SM. Finite element optimization of finite stepped slider bearing profiles. ASLE Trans 1974;17(2):105–10.

[6] Shen C, Khonsari MM. Numerical optimization of texture shape for parallel surfaces under unidirectional and bidirectional sliding. Tribol Int 2015;82:1–11.

[7] Etsion I, Burstein L. A model for mechanical seals with regular microsurface structure. Tribol Trans 1996;39(3):677–83.

[8] Fowell MT, Medina S, Olver AV, Spikes HA, Pegg IG. Parametric study of texturing in convergent bearings. Tribol Int 2012;52:7–16.

[9] Rahmani R, Shirvani A, Shirvani H. Optimization of partially textured parallel thrust bearings with square-shaped micro-dimples. Tribol Trans 2007;50(3):401–6.

[10] Morris N, Leighton M, De la Cruz M, Rahmani R, Rahnejat H, Howell-Smith S. Combined numerical and experimental investigation of the micro-hydrodynamics of chevron-based textured patterns influencing conjunctional friction of sliding contacts. Proc Inst Mech Eng J 2015;229(4):316–35.

[11] Vlădescu S, Ciniero A, Tufail K, Gangopadhyay A, Reddyhoff T. Optimisation of pocket geometry for friction reduction in piston-liner contacts. Tribol Trans 2017;(just-accepted).

[12] Profito FJ, Vlădescu S, Reddyhoff T, Dini D. Transient experimental and modelling studies of laser-textured micro-grooved surfaces with a focus on piston-ring cylinder liner contacts. Tribol Int 2017;113:125–36.

[13] Gropper D, Harvey TJ, Wang L. Numerical analysis and optimization of surface textures for a tilting pad thrust bearing. Tribol Int 2018;124:134–44.

[14] Codrignani A, Frohnapfel B, Magagnato F, Schreiber P, Schneider J, Gumbsch P. Numerical and experimental investigation of texture shape and position in the macroscopic contact. Tribol Int 2018;122:46–57.

[15] Teo W, Dolatabadi N, Rahmani R, Morris N, Rahnejat H. Combined analytical and experimental evaluation of frictional performance of lubricated untextured and partially textured sliders. Lubricants 2018;6(4):88.

[16] Pascovici MD, Cicone T, Fillon M, Dobrica MB. Analytical investigation of a partially textured parallel slider. Proc Inst Mech Eng J 2009;223(2):151–8.

[17] Rahmani R, Mirzaee I, Shirvani A, Shirvani H. An analytical approach for analysis and optimisation of slider bearings with infinite width parallel textures. Tribol Int 2010;43(8):1551–65.

[18] Dobrica MB, Fillon M, Pascovici MD, Cicone T. Optimizing surface texture for hydrodynamic lubricated contacts using a mass-conserving numerical approach. Proc Inst Mech Eng J 2010;224(8):737–50.

[19] Guzek Agata, Podsiadlo Pawel, Stachowiak Gwidon W. Optimization of textured surface in 2D parallel bearings governed by the reynolds equation including cavitation and temperature. Tribol Online 2013;8(1):7–21.

[20] Fesanghary M, Khonsari MM. On the shape optimization of self-adaptive grooves. Tribol Trans 2011;54(2):256–64.

[21] Wang N, Ho C, Cha K. Engineering optimum design of fluid-film lubricated bearings. Tribol Trans 2000;43(3):377–86.

[22] Maday CJ. A bounded variable approach to the optimum slider bearing. J Lubr Technol 1968;90(1):240–2.

[23] Maday CJ. The maximum principle approach to the optimum one-dimensional journal bearing. J Lubr Technol 1970;92(3):482–7.

[24] Alyaqout SF, Elsharkawy AA. Optimum shape design for surface of a thermohydrodynamic lubrication slider bearing. Lubricat Sci 2013;25(6):379–95.

[25] Nocedal J, Wright S. Numerical optimization. Springer Science & Business Media; 2006.

[26] Lions JL. Optimal control of systems governed by partial differential equations problèmes aux limites. Springer; 1971.

[27] Giles MB, Pierce NA. An introduction to the adjoint approach to design. Flow Turbul Combust 2000;65(3–4):393–415.

[28] Jameson Antony. Aerodynamic design via control theory. J Sci Comput 1988;3(3):233–60.

[29] Reuther J J, Jameson A, Alonso JJ, Rimlinger MJ, Saunders D. Constrained multipoint aerodynamic shape optimization using an adjoint formulation and parallel computers, part 1. J Aircraft 1999;36(1):51–60.

[30] Yoon SJ, Choi DH. Adjoint design sensitivity analysis of molecular gas film lubrication sliders. J Tribol 2003;125(1):145–51.

[31] van Ostayen Ron AJ, van Beek Anton, Munnig-Schmidt Rob H. Film height optimization of hydrodynamic slider bearings. In: ASME/STLE 2007 international joint tribology conference. American Society of Mechanical Engineers Digital Collection; 2009, p. 237–9.

[32] Van Ostayen RAJ. Film height optimization of dynamically loaded hydrodynamic slider bearings. Tribol Int 2010;43(10):1786–93.

[33] COMSOL AB, Stockholm, Sweden. COMSOL multiphysics® v. 5.4. www.comsol.com.

[34] Braun D, Greiner C, Schneider J, Gumbsch P. Efficiency of laser surface texturing in the reduction of friction under mixed lubrication. Tribol Int 2014;77:142–7.

[35] Adjemout M, Brunetiere N, Bouyer J. Numerical analysis of the texture effect on the hydrodynamic performance of a mechanical seal. Surface Topogr Metrol Prop 2015;4(1):014002.

[36] Woloszynski T, Podsiadlo P, Stachowiak GW. Efficient solution to the cavitation problem in hydrodynamic lubrication. Tribol Lett 2015;58(1):18.

[37] Elrod HG. A computer program for cavitation and starvation problems. Cavitation Relat Phenom Lubr 1974;37.

[38] Olsson K. Cavitation in dynamically loaded bearing. Trans Chalmers Univ Tech Sweden 1957;308.

[39] Bertocchi L, Dini D, Giacopini M, Fowell M T, Baldini A. Fluid film lubrication in the presence of cavitation: a mass-conserving two-dimensional formulation for compressible, piezoviscous and non-Newtonian fluids. Tribol Int 2013;67:61–71.

[40] Sahlin F, Almqvist A, Larsson R, Glavatskih S. A cavitation algorithm for arbitrary lubricant compressibility. Tribol Int 2007;40(8):1294–300.

[41] Rahmani R, Shirvani A, Shirvani H. Analytical analysis and optimisation of the Rayleigh step slider bearing. Tribol Int 2009;42(5):666–74.

[42] Bradley AM. Pde-constrained optimization and the adjoint method. Tutorial; 2010.

[43] Bletzinger KU. A consistent frame for sensitivity filtering and the vertex assigned morphing of optimal shape. Struct Multidiscip Optim 2014;49(6):873–95.

[44] Stück A, Rung T. Adjoint RANS with filtered shape derivatives for hydrodynamic optimisation. Comput & Fluids 2011;47(1):22–32.

[45] Slawig T. PDE-Constrained control using f emlab–control of the Navier–Stokes equations. Numer Algorithms 2006;42(2):107–26.

[46] Nadarajah S, Jameson A. Studies of the continuous and discrete adjoint approaches to viscous automatic aerodynamic shape optimization. In 15th AIAA computational fluid dynamics conference; 2001. p. 2530.

[47] Siripuram RB, Stephens LS. Effect of deterministic asperity geometry on hydrodynamic lubrication. J Tribol 2004;126(3):527–34.

[48] Gherca A, Fatu A, Hajjam M, Maspeyrot P. Effects of surface texturing in steady-state and transient flow conditions: Two-dimensional numerical simulation using a mass-conserving cavitation model. Proc Inst Mech Eng J 2015;229(4):505–22.

[49] Aggarwal S, Pandey RK. Frictional and load-carrying behaviours of micro-textured sector shape pad thrust bearing incorporating the cavitation and thermal effects. Lubricat Sci 2017;29(4):255–77.

[50] Nanbu T, Ren N, Yasuda Y, Zhu Dg, Wang QJ. Micro-textures in concentrated conformal-contact lubrication: effects of texture bottom shape and surface relative motion. Tribol Lett 2008;29(3):241–52.

[51] Dobrica MB, Fillon M. About the validity of Reynolds equation and inertia effects in textured sliders of infinite width. Proc Inst Mech Eng J 2009;223(1):69–78.

[52] Brunetière N, Tournerie B. Numerical analysis of a surface-textured mechanical seal operating in mixed lubrication regime. Tribol Int 2012;49:80–9.

[53] Ramesh A, Akram W, Mishra SP, Cannon AH, Polycarpou AA, King WP. Friction characteristics of microtextured surfaces under mixed and hydrodynamic lubrication. Tribol Int 2013;57:170–6.

[54] Wang Zhuo, Wang Cheng-Wei, Wang Min, Zhao Quan-Zhong. Manipulation of tribological properties of stainless steel by picosecond laser texturing and quenching. Tribol Int 2016;99:14–22.

[55] Wang Xincai, Zheng Hongyu, Wan Yinchi, Feng Wenhe, Lam Yee Cheong. Picosecond laser surface texturing of a Stavax steel substrate for wettability control. Engineering 2018;4(6):816–21.

[56] Habchi W. A fully-coupled finite element model for the solution of thermal elastohydrodynamic lubrication problems. 2019.

[57] Larsson R. Modelling the effect of surface roughness on lubrication in all regimes. Tribol Int 2009;42(4):512–6.

[58] de Kraker A, van Ostayen RAJ, van Beek A, Rixen DJ. A multiscale method modeling surface texture effects. J Tribol 2007;129:1–10.

[59] Codrignani A, Savio D, Magagnato F, Frohnapfel B. A scaling parameter for pressure losses and thermal effects in lubricant flows with viscous dissipation. Tribol Int 2017;113:238–44.

[60] Arghir M, Alsayed A, Nicolas D. The finite volume solution of the Reynolds equation of lubrication with film discontinuities. Int J Mech Sci 2002;44(10):2119–32.